# UC Berkeley

Title

Superlattice-induced ferroelectricity in charge-ordered La1/3Sr2/3FeO3

Permalink

https://escholarship.org/uc/item/9hm6d5v6

Journal

Proceedings of the National Academy of Sciences of the United States of America, 116(48)

ISSN

0027-8424

Authors

Park, Young
Rabe, Karin M
Neaton, Jeffrey B

Publication Date

2019-11-26

DOI

10.1073/pnas.1906513116

Peer reviewed

# Superlattice-induced ferroelectricity in charge-ordered $La_{1/3}Sr_{2/3}FeO_3$

Se Young Park[a,b,c], Karin M. Rabe[d,1], and Jeffrey B. Neaton[c,e,f]

[a]Center for Correlated Electron Systems, Institute for Basic Science, Seoul 08826, Republic of Korea; [b]Department of Physics and Astronomy, Seoul National University, Seoul 08826, Republic of Korea; [c]Department of Physics, University of California, Berkeley, CA 94720; [d]Department of Physics & Astronomy, Rutgers University, Piscataway, NJ 08854; [e]Molecular Foundry, Lawrence Berkeley National Laboratory, Berkeley, CA 94720; and [f]Kavli Energy NanoScience Institute, University of California, Berkeley, CA 94720

**Charge-order–driven ferroelectrics are an emerging class of functional materials, distinct from conventional ferroelectrics, where electron-dominated switching can occur at high frequency. Despite their promise, only a few systems exhibiting this behavior have been experimentally realized thus far, motivating the need for new materials. Here, we use density-functional theory to study the effect of artificial structuring on mixed-valence solid-solution $La_{1/3}Sr_{2/3}FeO_3$ (LSFO), a system well studied experimentally. Our calculations show that A-site cation (111)-layered LSFO exhibits a ferroelectric charge-ordered phase in which inversion symmetry is broken by changing the registry of the charge order with respect to the superlattice layering. The phase is energetically degenerate with a ground-state centrosymmetric phase, and the computed switching polarization is 39 $\mu C/cm^2$, a significant value arising from electron transfer between $FeO_6$ octahedra. Our calculations reveal that artificial structuring of LSFO and other mixed valence oxides with robust charge ordering in the solid solution phase can lead to charge-order–induced ferroelectricity.**

ferroelectricity | density-functional theory | perovskite-oxide superlattices | charge ordering

The formulation of new design principles for ferroelectric materials has recently attracted great interest. A broad principle, proposed in refs. 1 and 2, is to start with a high-symmetry reference phase and combine 2 symmetry-breaking orderings, neither of which separately lifts inversion symmetry, to generate 2 or more polar variants. Perovskite oxides are ideal systems to search for realizations of mechanisms governed by the abovementioned broad principle. They exhibit various symmetry-lowering lattice instabilities as well as magnetic, charge and orbital ordering in bulk phases (3–5). Furthermore, with the recent progress in atomic-scale layer-by-layer growth techniques, symmetry-breaking compositional order can be achieved in a wide variety of complex oxide systems via superlattices (6–9). The combination of orderings has thus been the basis of discovery of several new types of perovskite ferroelectrics. In particular, in hybrid improper ferroelectricity (10), a lattice distortion that preserves inversion symmetry (typically an oxygen-octahedron rotation-tilt pattern) combines with symmetry breaking by layering, either in a Ruddlesden–Popper phase (10) or in a perovskite $ABO_3/A'BO_3$ (001) superlattice (11–13), generating polar variants. In these systems, the switching polarization is generated by a polar lattice distortion in the lowered-symmetry state.

Charge-order–driven ferroelectricity can be obtained by combining symmetry breaking by charge ordering with symmetry breaking by layered cation ordering to generate polar variants (14–16). For example, in the 1:1 superlattice $LaVO_3/SrVO_3$, layered charge ordering of $V^{3+}$ and $V^{4+}$ combines with the layered ordering of La and Sr to break up–down symmetry normal to the layers, generating 2 polar variants (16). The distinctive characteristic differentiating charge-order–driven ferroelectric-

ity from the displacive type is that the switching polarization arises primarily from interionic transfer of electrons when the charge ordering pattern is switched. This is accompanied by a small polar lattice distortion, which can be used as a proxy to signal the polar nature of the phase. Such electronic ferroelectrics might be useful for high-frequency switching devices given that the polarization switching timescale is not limited by phonon frequency (17, 18).

To promote experimental observation of switchable polarization due to charge-order–driven ferroelectricity, the system should exhibit a strong tendency to charge disproportionation. Further, there should be a strong tendency to charge ordering, which could be manifested as robust charge ordering already in the solid solution phase. The iron-oxide family is a class of materials that satisfies these conditions. Unlike $La_{1/2}Sr_{1/2}VO_3$, in which no charge ordering is observed in the solid solution down to low temperatures (19), robust charge orderings are observed in many iron oxides such as magnetite (20), hexagonal ferrite $LuFe_2O_4$ (21), and perovskite $CaFeO_3$ (22) and $La_{1/3}Sr_{2/3}FeO_3$ solid solution (23).

Perovskite solid solution $La_{1/3}Sr_{2/3}FeO_3$ (LSFO) has a charge-ordered Mott-insulating state as the low-temperature phase. The average valence of Fe is +3.67 assuming +2, +3, and −2 charge states for Sr, La, and O, respectively. For

---

**Significance**

Charge-order–driven ferroelectrics are an emerging class of materials with promise for high-frequency electron-dominated polarization switching, distinct from conventional ferroelectrics. However, only a few systems exhibiting this behavior have been experimentally realized thus far. With continued development of layer-by-layer growth techniques with a high level of composition control, the exploration of charge-ordered ferroelectrics can be extended to artificially structured superlattices. Here, we use density-functional theory to explore an experimentally realized bulk perovskite iron-oxide solid solution with robust charge ordering and find that in superlattices formed by layered cation ordering, bulk charge ordering is maintained and can lead to charge-order–driven ferroelectricity. Our results suggest that other broad classes of mixed valence materials may be promising candidates for discovery of electronic ferroelectrics.

**Fig. 1.** (*A*) Atomic arrangement of $La_{1/3}Sr_{2/3}FeO_3$ solid solution with charge and magnetic ordering. Light blue and magenta colors are for Fe ions and surrounding oxygen octahedron of $Fe^{3+}$ and $Fe^{5+}$, respectively. The silver and black spheres represent the La or Sr atoms occupying 2 distinct Wyckoff positions (2*a* and 4*d*) of the $P\bar{3}c1$ space group with multiplicity of 2 and 4, respectively. (*B*) Top view showing the $a^-a^-a^-$ oxygen-octahedron rotation pattern. (*C*) Side view showing the antiphase antiferromagnetic ordering.

T > 210 K, LSFO is metallic with all Fe sites equivalent. Below 210 K, a metal–insulator transition is observed with the onset of both antiferromagnetic (AF) and charge ordering (CO) where 2 distinct charge states are stabilized by the breathing distortion of the oxygen octahedra (23–25). Nominally this charge ordering corresponds to $3Fe^{3.67+} = Fe^{5+} + 2Fe^{3+}$, but due to the strong hybridization of Fe-$d$ $e_g$ states and the surrounding oxygen ligands, the configurations include some ligand hole character (26) and indeed the measured magnetic moments of $Fe^{3+}/Fe^{5+}$ states are lower than the nominal values (23, 25, 27). However, for convenience we continue to refer to these charge states as $Fe^{3+}$ and $Fe^{5+}$. Fig. 1*A* describes the crystal structure with the observed charge-ordering pattern, in which each charge state forms a (111) plane stacked in the repeated pattern of $Fe^{5+}$-$Fe^{3+}$-$Fe^{3+}$. The magnetic moments order ferromagnetically within each (111) plane. In the out-of-plane direction, the moments order in an antiphase antiferromagnetic (APAF) pattern in which the moments in adjacent planes with the same charge state are antialigned and the moments in adjacent planes with different charge states are aligned, as illustrated in Fig. 1*C*. Experimentally, (001)- and (111)-oriented thin films and (001)-oriented superlattices are reported, with resistivity measurements consistent with a charge-ordered Mott-insulating state as the low-temperature phase (28, 29).

Charge ordering in LSFO has been the subject of investigation through first-principles calculations (26, 29–31), with disproportionation to $Fe^{3+}/Fe^{5+}$ observed when on-site electron correlation is included via a Hubbard $U$ parameter (30). These studies have considered various ordering patterns for La/Sr and their effects on charge disproportionation, charge ordering, and magnetic ordering of the electronic ground state (29–31). The energetics of the system are found to be driven by magnetic exchange, with both lattice distortion and correlation needed to produce an insulating ground state.

In this paper, using symmetry analysis and first-principles density-functional theory (DFT) results, we find that a layered superlattice ordering of La/Sr cations in charge-ordered $La_{1/3}Sr_{2/3}FeO_3$ generates electronic ferroelectricity via the combined symmetry breaking of charge ordering and cation layering. Depending on the registry between the superlattice layering and the charge-ordering patterns, both centrosymmetric and ferroelectric phases can be stabilized. Electronic and structural properties of the low-energy phases and details of switching between 2 polar branches are presented. This example serves

as a proof of concept for this design principle, which can be more broadly applied in the search for electronic ferroelectricity in chemically complex perovskite-oxide solid solutions with multiple valence cations.

Our analysis of the symmetry breaking by charge ordering and cation ordering in this system starts with the atomic arrangement in the LSFO solid solution shown in Fig. 1. The corner-connected octahedra of the perovskite structure are rotated in the $a^-a^-a^-$ pattern with La/Sr ions in between the Fe-centered octahedral cages, forming a triangular lattice as viewed along the $c$ (pseudocubic [111]) direction (Fig. 1*B*). This high-symmetry phase has space group $R\bar{3}c$, with all Fe sites equivalent and all A cation sites equivalent. We analyze the symmetry lowering due to the charge and cation orderings in Fig. 2. First, we introduce the experimentally observed (111)-oriented charge ordering, which lowers the space group symmetry to $P\bar{3}c1$ in which there are 2 Wyckoff positions for A-site ions (2*a*, 4*d*), represented as silver and black spheres in Fig. 1*A*. Next, we introduce layered A-site cation orderings. Following the (111)-oriented charge ordering, relevant A-site orderings are expected to be (111) oriented and thus can be expressed within the 30-atom unit cell. To maintain the same average valence for Fe-$d$ states, the superlattice needs to satisfy the constraint of 1:2 ratio of La and Sr. This yields 2 types of atomic arrangements: one maintaining the same symmetry by assigning La to 2*a* (with multiplicity 2) and Sr to 4*d* (with multiplicity 4) Wyckoff positions and the other lowering symmetry by assigning more than one atomic species to the 2*a* and/or 4*d* Wyckoff position. The first type, illustrated in Fig. 2, *Bottom Left*, is clearly unique and does not break any additional symmetry. The latter type allows for many possible arrangements, but there is only one arrangement, shown in Fig. 2, *Bottom Right*, that has uniformly separated La-(111) planes which, as observed for the (001)-oriented superlattice (29), maintains the charge-ordering pattern. For this arrangement, the space group symmetry is lowered to noncentrosymmetric $P3c1$, demonstrating the possibility of superlattice-driven ferroelectricity in the presence of charge ordering.

Fig. 3 shows the charge-ordering patterns for the centrosymmetric $P\bar{3}c1$ phase (Fig. 3*A*) and the 2 polar variants of the
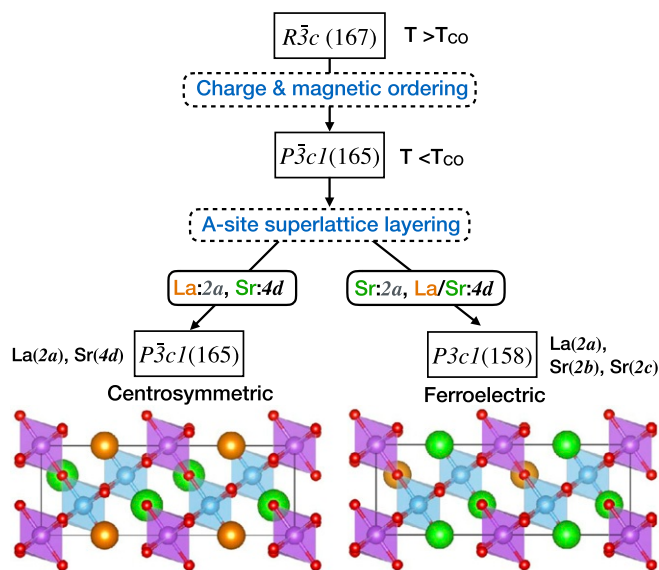


**Fig. 2.** Space group analysis of symmetry lowering in the LSFO solution. Starting from the high-temperature $R\bar{3}c$ structure, the charge ordering lowers the symmetry to the $P\bar{3}c1$ space group. From there, different superlattice layering arrangements described in the text produce centrosymmetric and ferroelectric phases.
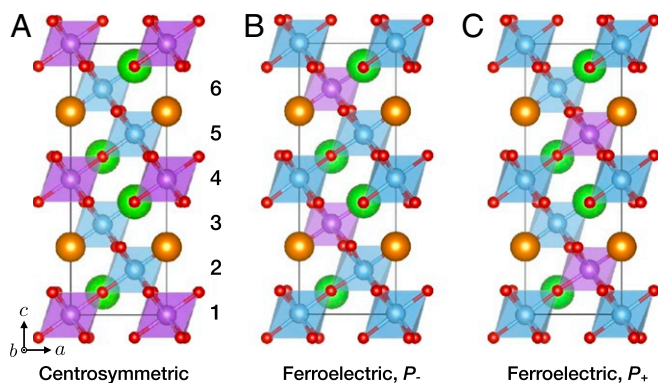
**Fig. 3.** Three charge-ordering patterns for A-cation ordered superlattices. (*A*) Centrosymmetric charge-ordering pattern. (*B* and *C*) Ferroelectric charge-ordering patterns with 2 polar variants in which $P_+/P_-$ are related by inversion. The Fe layers are numbered 1 to 6. For both the centrosymmetric and the ferroelectric phases, the *c*-axis rotations of the octahedra in layers 1, 2, and 3 are opposite to those in layers 4, 5, and 6, respectively.

ferroelectric $P3c1$ phase (Fig. 3 *B* and *C*). We can see that the main difference between the centrosymmetric and ferroelectric phases is the registry of the charge ordering with respect to A-site layered ordering. This suggests that electric-field–controlled switching from the centrosymmetric to the ferroelectric phase or between 2 polar variants in the ferroelectric phase can occur through charge transfer between Fe sites.

With first-principles calculations, we now investigate the total energies and structural parameters of these superlattice phases. In addition, we check the assumption that the charge-ordering pattern of the solid solution is maintained in the A-site ordered structures. We generate the alternative charge- and magnetic-ordering patterns to be considered through a systematic symmetry analysis. The details of this analysis and of the first-principles approach are discussed in *SI Appendix*.

Table 1 summarizes the low-energy phases identified. The lowest-energy phase is the centrosymmetric (CS) $P\bar{3}c1$ phase (Fig. 3*A*) with $Fe^{3+}/Fe^{5+}$ charge ordering and APAF magnetic ordering; it is an insulator with a DFT$+U$ band gap of 0.3 eV, in reasonable agreement with the experimentally measured band gap (0.13 eV) (32). This charge-ordering and magnetic-ordering pattern is identical to that observed in the solid solution, confirming the hypothesis that the charge and magnetic ordering would be insensitive to the A-site ordering. The oxygen octahedral volume in the relaxed structure of the CS-APAF phase is 9.5 $Å^3$ for $Fe^{5+}$ and 10.5 $Å^3$ for $Fe^{3+}$, showing the breathing distortion. The $Fe^{3+}$ ions shift about 0.01 Å from the center of the octahedron toward the La plane. The ferroelectric (FE) $P3c1$ phase (Fig. 3 *B* and *C*) with the same APAF magnetic ordering is only

0.54 meV per Fe higher in energy, with octahedral distortions and magnetic moments for $Fe^{3+}$ and $Fe^{5+}$ virtually identical to those in the CS-APAF phase. With respect to the electrostatic energy, the main difference between the 2 different registries of the charge-ordering pattern with respect to the A-site layered ordering is that in the CS phase, an $Fe^{5+}$ plane lies between the 2 adjacent $Sr^{2+}$ layers, while in the FE phase, the $Fe^{5+}$ plane lies between a $Sr^{2+}$ and a $La^{3+}$ layer, with a nominally higher electrostatic energy. The tiny computed energy difference implies substantial screening from the oxygen ligands, also seen in other charge-order–induced ferroelectric materials (16). As a result, it should be possible to switch this system to a polar variant with an applied external field with retention of the polar structure when the field is removed, producing a ferroelectric $P–E$ hysteresis loop.

Considering magnetic-ordering patterns, for AF and ferrimagnetic (Fi) ordering, we find charge-ordered insulating phases substantially higher in energy (>100 meV per Fe) than the CS-APAF phase. The energy increase on changing the magnetic-ordering patterns is consistent with the Goodenough–Kanamori–Anderson rule (33–35) favoring APAF magnetic ordering. By comparing the total energies of CS-APAF, CS-AF, and CS-Fi phases and assuming $S = 5/2$ for $Fe^{3+}$ and $S = 3/2$ for $Fe^{5+}$, we calculate the nearest-neighbor exchange coupling constants for $Fe^{3+}$-$Fe^{5+}$ and $Fe^{3+}$-$Fe^{3+}$ pairs to be $-8.3$ meV and 9.5 meV, respectively, showing strong magnetic interactions consistent with inelastic neutron scattering measurements (25). For ferromagnetic (F) ordering, we find a metallic $P\bar{3}c1$ phase with no charge ordering or breathing distortions at an energy of 24 meV per Fe above the CS-APAF phase, in contrast to pure $CaFeO_3$, in which a ferromagnetic $Fe^{3+}/Fe^{5+}$ insulating charge-ordered state is found as the ground state (36, 37).

To investigate the robustness of the $Fe^{3+}/Fe^{5+}$ (111) charge ordering, we consider states with other ordering patterns and disproportionation. Considering states with $Fe^{3+}/Fe^{5+}$ charge ordering in the (111) plane, we find a locally stable charge-ordered phase with APAF magnetic ordering that has a significantly higher total energy of about 67 meV per Fe relative to the CS-APAF phase (see *SI Appendix* for details). By assuming a different disproportionation $Fe^{3+}/Fe^{4+}$, we find a locally stable CS-Fi phase, higher in total energy by 51 meV per Fe, which is metallic (last column of Table 1). We note that this phase has doubly degenerate bands along high-symmetry lines crossing the Fermi energy. As discussed in more detail in *SI Appendix*, these degeneracies are protected by inversion symmetry, and breaking the inversion symmetry by changing the registry of the superlattice layering and the charge order leads to the FE-Fi2 phase, opening a band gap.

Fig. 4*A* shows the projected density of states (PDOS) of the CS-APAF phase. We find that the PDOS of the FE-APAF phase (Fig. 4*B*) is almost identical to that of the CS-APAF phase, consistent with the small energy and structural difference,

**Table 1. Low-energy phases of LSFO (111) superlattice**

| Charge states | $2Fe^{5+}(d^3)/4Fe^{3+}(d^5)$ | | | | | | $6Fe^{3.67+}(d^{4.33})$ | $2Fe^{3+}(d^5)/4Fe^{4+}(d^4)$ |
|---|---|---|---|---|---|---|---|---|
| CO patterns | CS | FE | CS | FE | CS | FE | CS | CS |
| $\Delta E$/Fe, meV | 0 | 0.54 | 124 | 119 | 243 | 42 | 24 | 51 |
| Phase | I | I | I | I | I | I | M | M |
| Magnetic ordering | APAF | APAF | AF | AF | Fi | Fi2 | F | Fi |
| | ⇑⇑⇓⇓⇑⇑ | ⇑⇑⇑⇓⇓⇓ | ⇑⇓⇑⇓⇑⇓ | ⇑⇓⇑⇓⇑⇓ | ⇑⇓⇑⇓⇓⇓ | ⇑⇑⇓⇑⇓⇑ | ⇑⇑⇑⇑⇑⇑ | ⇑⇑⇓⇑⇓⇓ |
| $m$ [Fe1/Fe2/Fe3], $\mu_B$ | 3.5/4.0/4.0 | 4.0/3.5/4.0 | 2.8/4.1/4.1 | 4.1/2.9/4.1 | 2.7/4.2/4.2 | 3.9/4.1/3.3 | 4.0/4.0/4.0 | 4.1/3.7/3.7 |

For each phase, the charge ordering, total energy per Fe, electronic character, magnetic ordering, and magnetic moments are given. I and M denote insulator and metal, respectively. The symbols F, AF, Fi, and APAF denote ferromagnetic, antiferromagnetic, ferrimagnetic, and antiphase–antiferromagnetic ordering, respectively. For the magnetic-ordering patterns, the arrows represent spin directions and magnitude in which the double arrows denote the $Fe^{3+}$ charge state and single arrows denote the other charge states ($Fe^{5+}$ or $Fe^{4+}$). The calculated magnetic moments presented are for the first 3 Fe sites.
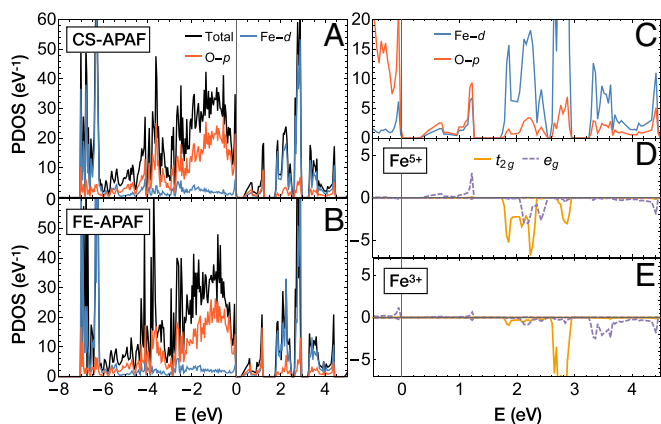
**Fig. 4.** Total density of states (black line) and orbital PDOS for Fe-$d$ (blue) and O-$p$ (red) orbitals of CS-APAF (*A*) and FE-APAF (*B*) phases. (*C*) Close-up of PDOS for the unoccupied states. (*D*) PDOS of unoccupied $t_{2g}$ and $e_g$ states for the spin-up $Fe^{5+}$ site. (*E*) PDOS of unoccupied $t_{2g}$ and $e_g$ states for the spin-up $Fe^{3+}$ site.

noting that the band gap is slightly smaller (0.24 eV). The valence bands are mainly derived from O-$p$ bands located above the occupied Fe-$d$ bands around $-7$ eV and the conduction bands consist mostly of Fe-$d$ derived bands with a band gap about 0.3 eV, showing that this is a charge-transfer insulator (38). We find that the low-lying unoccupied bands around 1 eV have strong hybridization between Fe-$d$ and O-$p$ states (Fig. 4*C*), supporting the strong screening by the oxygen ligand holes, previously discussed for the solid solution (26, 39). From the PDOS of $Fe^{5+}$ (Fig. 4*D*), we find that the relevant Fe-$d$ states are $e_g$. The PDOS of $Fe^{3+}$ (Fig. 4*E*) shows negligible occupation of spin-up states, consistent with a fully spin-polarized $d^5$ state.

Next, we consider the switching between the 2 inversion-related polar variants shown in Fig. 5*A* by computing energy, band gap, magnetic moments, and polarization for fixed atomic arrangements obtained by linearly interpolating between those of the 2 variants, parameterized by $0 \leq \lambda \leq 1$. As shown in Fig. 5*B*, the calculated energy barrier along the path is 25 meV per Fe; this is smaller than the barriers calculated for small polaron hopping for $Li_xFePO_4$ (88 to 108 meV) and hematite (85 to 120 meV) (40, 41) and only slightly larger than the computed double-well potential depth in the conventional ferroelectric $BaTiO_3$ (20 meV) (42). For $0 \leq \lambda \leq 0.5$, the charge-ordering pattern is that of the $\lambda = 0$ polar variant and the magnetic moments change by relatively small amounts. Similarly, for $0.5 \leq \lambda \leq 1$, the charge-ordering pattern of the $\lambda \leq 1$ variant is maintained. Exactly at $\lambda = 0.5$, with centrosymmetric atomic arrangements, we find 2 degenerate states with broken inversion symmetry, one with the change ordering of the $\lambda = 0$ polar variant and the other with the charge ordering of the $\lambda = 1$ polar variant. The cusp in the Born–Oppenheimer energy surface indicates a first-order transition between the 2 polar branches, with a band gap $> 70$ meV maintained along the transition path (Fig. 5*C*). We note that due to the small band gap, leakage currents may be generated during the switching process, which could hinder the polarization switching. The first-order nature of the transition can be also seen from the magnetic moments of the Fe ions, with discontinuous jumps at $\lambda = 0.5$ from the nominal $2e^-$ charge transfer (Fig. 5*D*). This coincides with the discontinuous jump in the polarization, shown in Fig. 5*E* corresponding to a charge transfer of $2e^-$ across the La layer. This is supported by the Wannier center interpretation of the switching polarization in that 2 Wannier centers shift from one Fe site to the other at $\lambda = 0.5$, while the shifts in other Wannier centers do not con-

tribute significantly to the net polarization. We note that the shifts in Wannier centers associated with hybridized Fe-$d$ O-$p$ states do contribute to the calculated Born effective charges, as discussed in more detail in *SI Appendix* (43). The magnitude of the switching polarization is 39 $\mu C/cm^2$, comparable to $2P_s = 54 \mu C/cm^2$ of $BaTiO_3$.

For extending this mechanism beyond LSFO, we note that robust checkerboard ((111)-layered) charge ordering is reported in a wide range of perovskite oxides. In this case, (111)-layered A-cation ordering can remove the inversion center of the charge-ordered structure. Alternating single A and A′ layers results in the noncentrosymmetric $F\bar{4}3m$ (216) space group, the same as that of the cubic double-perovskite AA′BB′$O_6$. However, this space group is in fact nonpolar due to the presence of 2-fold rotation symmetries and the resulting phase is not ferroelectric. The combination of checkerboard charge ordering with 2 A layers alternating with A′ layers results in a centrosymmetric $P\bar{3}m1$ (164) space group, with an inversion center on one of the B sites. Other cation layering sequences and/or inclusion of additional symmetry-breaking distortions such as oxygen octahedron rotations could result in a polar space group; this is the subject of future work.

In conclusion, we propose a design principle for charge-order–induced ferroelectricity by artificial structuring of mixed valence oxides with robust charge ordering in the solid solution phase. We have demonstrated this principle for charge-ordered Mott-insulating $La_{1/3}Sr_{2/3}FeO_3$ solid solution in which a substantial switching polarization is predicted due to charge transfer between $FeO_6$ octahedra. Our approach is not limited to perovskite oxides and can be applied to broad classes of mixed valence materials to identify electronic ferroelectrics, potentially useful for applications requiring high-frequency switching properties.
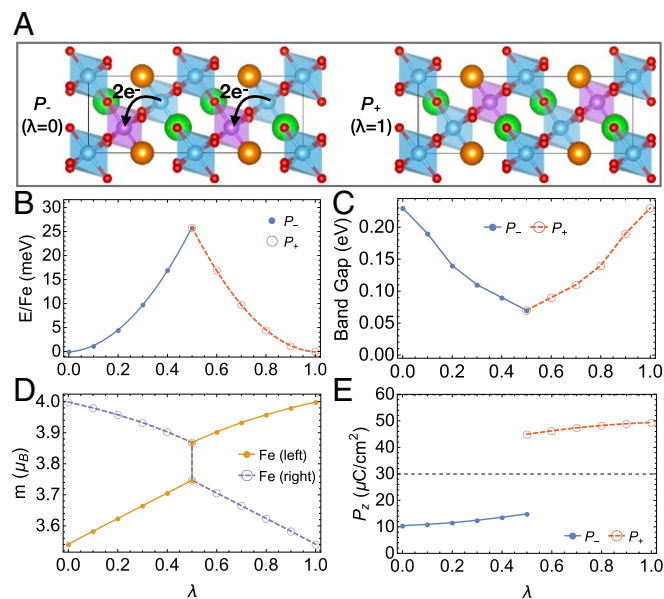


**Fig. 5.** (*A*) Atomic arrangements of 2 inversion-related polar variants, $P_-$ and $P_+$, showing the electron transfer relating the two. (*B*) Total energy per Fe for atomic arrangements linearly interpolated between those of the 2 polar variants shown in *A*. The zero of energy is taken as the energy of the 2 polar variants. $\lambda$ is the interpolation parameter ranging from $\lambda = 0$ for $P_-$ to $\lambda = 1$ for $P_+$. (*C*) $\lambda$ dependence of the DFT+$U$ band gap. (*D*) $\lambda$ dependence of the magnetic moments of the 2 Fe sites adjacent to the La layer (A, *Left* and *Right*). (*E*) $\lambda$ dependence of the polarization parallel to the $c$ axis assuming a branch choice corresponding to the electron transfer in *A*. The dashed line is drawn at half the quantum of polarization, for reference.

## Materials and Methods

We perform first-principles density-functional theory calculations with the generalized gradient approximation plus $U$ (GGA+$U$) method using the Vienna ab initio simulation package (44, 45). The Perdew–Becke–Erzenhof parameterization (46) for the exchange-correlation functional and the rotationally invariant form of the on-site Coulomb interaction (47) are used with $U = 5.4$ eV and $J = 1.0$ eV for the iron $d$ consistent with the values used in previous work [$U_{eff}(=U - J) = 4.4$ eV (29), $U = 5$ eV, $J = 1$ eV (30, 31)] and $U_f = 11$ eV and $J_f = 0.68$ eV for the La $f$ states to shift the La $f$ bands away from the Fermi energy (48). The charge-ordering pattern is determined through Wannier center analysis using the Wannier90 package (49). We find that the stability of $Fe^{3+}/Fe^{5+}$ charge ordering with APAF magnetic ordering is insensitive to the $U$ values over a broad range (*SI Appendix*). We used the projector-augmented wave method (50) with pseudopotentials containing 6 valence electrons for O ($2s^2 2p^4$), 14 for Fe ($3p^6 3d^7 4s^1$), 11 for La ($5s^2 5p^6 5d^1 6s^2$), and 10 for Sr ($4s^2 4d^6 5s^2$). For each charge-ordering pattern, we construct a starting crystal structure with breathing distortions corresponding to the charge-ordering pattern (see *SI Appendix* for further details). A $\sqrt{2} \times \sqrt{2} \times 2\sqrt{3}$ simple hexagonal unit cell with 6 Fe atoms is chosen to accommodate the relevant octahedral rotation distortions and charge-order patterns. An energy cutoff of 600 eV, $k$-point sampling on a $\Gamma$-centered $6 \times 6 \times 3$ grid, and a force threshold of 0.01 eV/Å are used for full structural relaxation. The spontaneous polarization is calculated using the Berry phase method (51) with an $8 \times 8 \times 4$ $k$-point grid.

**Data Availability.** All data needed to evaluate the conclusions in this paper are present in the main text and/or *SI Appendix*.

1. D. V. Efremov, J. van den Brink, D. I. Khomskii, Bond- versus site-centred ordering and possible ferroelectricity in manganites. *Nat. Mater.* **3**, 853–856 (2004).
2. D. Khomskii, Multiferroics: Different ways to combine magnetism and ferroelectricity. *J. Magn. Magn. Mater.* **306**, 1–8 (2006).
3. M. Imada, A. Fujimori, Y. Tokura, Metal-insulator transitions. *Rev. Mod. Phys.* **70**, 1039–1263 (1998).
4. Y. Tokura, N. Nagaosa, Orbital physics in transition-metal oxides. *Science* **288**, 462–468 (2000).
5. D. I. Khomskii, *Transition Metal Compounds* (Cambridge University Press, 2014).
6. P. Zubko, S. Gariglio, M. Gabay, P. Ghosez, J. M. Triscone, Interface physics in complex oxide heterostructures. *Annu. Rev. Condens. Matter Phys.* **2**, 141–165 (2011).
7. H. Y. Hwang et al., Emergent phenomena at oxide interfaces. *Nat. Mater.* **11**, 103–113 (2012).
8. J. Chakhalian, J. W. Freeland, A. J. Millis, C. Panagopoulos, J. M. Rondinelli, *Colloquium*: Emergent properties in plane view: Strong correlations at oxide interfaces. *Rev. Mod. Phys.* **86**, 1189–1202 (2014).
9. J. Young, P. Lalkiya, I. M. Rondinelli, Design of noncentrosymmetric perovskites from centric and acentric basic building units. *J. Mater. Chem. C* **4**, 4016–4027 (2016).
10. N. A. Benedek, C. J. Fennie, Hybrid improper ferroelectricity: A mechanism for controllable polarization-magnetization coupling. *Phys. Rev. Lett.* **106**, 107204 (2011).
11. E. Bousquet et al., Improper ferroelectricity in perovskite oxide artificial superlattices. *Nature* **452**, 732–736 (2008).
12. N. A. Benedek, A. T. Mulder, C. J. Fennie, Polar octahedral rotations: A path to new multifunctional materials. *J. Solid State Chem.* **195**, 11–20 (2012).
13. J. Varignon, N. C. Bristowe, E. Bousquet, P. Ghosez, Coupling and electrical control of structural, orbital and magnetic orders in perovskites. *Sci. Rep.* **5**, 15364 (2015).
14. K. Yamauchi, T. Fukushima, S. Picozzi, Ferroelectricity in multiferroic magnetite $Fe_3O_4$ driven by noncentrosymmetric $Fe^{2+}/Fe^{3+}$ charge-ordering: First-principles study. *Phys. Rev. B* **79**, 212404 (2009).
15. K. Kobayashi et al., Electronic ferroelectricity in a molecular crystal with large polarization directing antiparallel to ionic displacement. *Phys. Rev. Lett.* **108**, 237601 (2012).
16. S. Y. Park, A. Kumar, K. M. Rabe, Charge-order-induced ferroelectricity in $LaVO_3$/$SrVO_3$ superlattices. *Phys. Rev. Lett.* **118**, 087602 (2017).
17. S. Ishihara, Electronic ferroelectricity and frustration. *J. Phys. Soc. Jpn.* **79**, 011010 (2010).
18. K. Yamauchi, P. Barone, Electronic ferroelectricity induced by charge and orbital orderings. *J. Phys. Condens. Matter* **26**, 103201 (2014).
19. F. Inaba, T. Arima, T. Ishikawa, T. Katsufuji, Y. Tokura, Change of electronic properties on the doping-induced insulator-metal transition in $La_{1-x}Sr_xVO_3$. *Phys. Rev. B* **52**, R2221–R2224 (1995).
20. E. J. W. Verwey, Electronic conduction of magnetite ($Fe_3O_4$) and its transition point at low temperatures. *Nature* **144**, 327–328 (1939).
21. N. Ikeda et al., Ferroelectricity from iron valence ordering in the charge-frustrated system $LuFe_2O_4$. *Nature* **436**, 1136–1138 (2005).
22. M. Takano, N. Nakanishi, Y. Takeda, S. Naka, T. Takada, Charge disproportionation in $CaFeO_3$ studied with the Mössbauer effect. *Mater. Res. Bull.* **12**, 923–928 (1977).
23. P. Battle, T. Gibb, P. Lightfoot, The structural consequences of charge disproportionation in mixed-valence iron oxides. I. The crystal structure of $Sr_2LaFe_3O_{8.94}$ at room temperature and 50 K. *J. Solid State Chem.* **84**, 271–279 (1990).
24. J. Q. Li, Y. Matsui, S. K. Park, Y. Tokura, Charge ordered states in $La_{1-x}Sr_xFeO_3$. *Phys. Rev. Lett.* **79**, 297–300 (1997).
25. R. J. McQueeney et al., Stabilization of charge ordering in $La_{1/3}Sr_{2/3}FeO_{3-\delta}$ by magnetic exchange. *Phys. Rev. Lett.* **98**, 126402 (2007).
26. J. Matsuno et al., Photoemission and Hartree-Fock studies of oxygen-hole ordering in charge-disproportioned $La_{1-x}Sr_xFeO_3$. *Phys. Rev. B* **60**, 4605–4608 (1999).
27. H. Wadati et al., Temperature-dependent soft x-ray photoemission and absorption studies of charge disproportionation in $La_{1-x}Sr_xFeO_3$. *J. Phys. Soc. Jpn.* **75**, 054704 (2006).
28. M. Minohara et al., Thickness-dependent physical properties of $La_{1/3}Sr_{2/3}FeO_3$ thin films grown on $SrTiO_3$ (001) and (111) substrates. *J. Appl. Phys.* **120**, 025303 (2016).
29. A. L. Krick, C. W. Lee, R. J. Sichel-Tissot, A. M. Rappe, S. J. May, Interplay between cation and charge ordering in $La_{1/3}Sr_{2/3}FeO_3$ superlattices. *Adv. Electron. Mater.* **2**, 1500372 (2016).
30. T. Saha-Dasgupta, Z. S. Popović, S. Satpathy, Density functional study of the insulating ground states in $CaFeO_3$ and $La_{1/3}Sr_{2/3}FeO_3$ compounds. *Phys. Rev. B* **72**, 045143 (2005).
31. Y. Zhu et al., Unconventional slowing down of electronic recovery in photoexcited charge-ordered $La_{1/3}Sr_{2/3}FeO_3$. *Nat. Commun.* **9**, 1799 (2018).
32. T. Ishikawa, S. K. Park, T. Katsufuji, T. Arima, Y. Tokura, Optical spectroscopy of charge-ordering transition in $La_{1/3}Sr_{2/3}FeO_3$. *Phys. Rev. B* **58**, R13326–R13329 (1998).
33. P. W. Anderson, Antiferromagnetism. Theory of superexchange interaction. *Phys. Rev.* **79**, 350–356 (1950).
34. J. B. Goodenough, Theory of the role of covalence in the perovskite-type manganites [La, $M$ (II)] $MnO_3$. *Phys. Rev.* **100**, 564–573 (1955).
35. J. Kanamori, Superexchange interaction and symmetry properties of electron orbitals. *J. Phys. Chem. Solids* **10**, 87–98 (1959).
36. A. Cammarata, J. M. Rondinelli, Spin-assisted covalent bond mechanism in "charge-ordering" perovskite oxides. *Phys. Rev. B* **86**, 195144 (2012).
37. Y. Zhang, M. M. Schmitt, A. Mercy, J. Wang, P. Ghosez, From charge- to orbital-ordered metal-insulator transition in alkaline-earth ferrites. *Phys. Rev. B* **98**, 081108 (2018).
38. J. Zaanen, G. A. Sawatzky, J. W. Allen, Band gaps and electronic structure of transition-metal compounds. *Phys. Rev. Lett.* **55**, 418–421 (1985).
39. J. B. Yang et al., Charge disproportionation and ordering in $La_{1/3}Sr_{2/3}FeO_{3-\delta}$. *J. Phys. Condens. Matter* **15**, 5093–5102 (2003).
40. T. Maxisch, F. Zhou, G. Ceder, *Ab initio* study of the migration of small polarons in olivine $Li_xFePO_4$ and their association with lithium ions and vacancies. *Phys. Rev. B* **73**, 104301 (2006).
41. N. Adelstein, J. B. Neaton, M. Asta, L. C. De Jonghe, Density functional theory based calculation of small-polaron mobility in hematite. *Phys. Rev. B* **89**, 245115 (2014).
42. R. E. Cohen, Origin of ferroelectricity in perovskite oxides. *Nature* **358**, 136–138 (1992).
43. K. Yamauchi, S. Picozzi, Mechanism of ferroelectricity in half-doped manganites with pseudocubic and bilayer structure. *J. Phys. Soc. Jpn.* **82**, 113703 (2013).
44. G. Kresse, J. Furthmüller, Efficient iterative schemes for *ab initio* total-energy calculations using a plane-wave basis set. *Phys. Rev. B* **54**, 11169–11186 (1996).
45. G. Kresse, D. Joubert, From ultrasoft pseudopotentials to the projector augmented-wave method. *Phys. Rev. B* **59**, 1758–1775 (1999).
46. J. P. Perdew, K. Burke, M. Ernzerhof, Generalized gradient approximation made simple. *Phys. Rev. Lett.* **77**, 3865–3868 (1996).
47. A. I. Liechtenstein, V. I. Anisimov, J. Zaanen, Density-functional theory and strong interactions: Orbital ordering in Mott-Hubbard insulators. *Phys. Rev. B* **52**, R5467–R5470 (1995).
48. M. T. Czyżyk, G. A. Sawatzky, Local-density functional and on-site correlations: The electronic structure of $La_2CuO_4$ and $LaCuO_3$. *Phys. Rev. B* **49**, 14211–14228 (1994).
49. A. A. Mostofi et al., An updated version of Wannier90: A tool for obtaining maximally-localised Wannier functions. *Comput. Phys. Commun.* **185**, 2309–2310 (2014).
50. P. E. Blöchl, Projector augmented-wave method. *Phys. Rev. B* **50**, 17953–17979 (1994).
51. R. D. King-Smith, D. Vanderbilt, Theory of polarization of crystalline solids. *Phys. Rev. B* **47**, 1651–1654 (1993).